Thin film bulk acoustic wave filters with ring-dot electrodes[*]

Jing LIU[1,2], Jian-ke DU[†‡1], Ji WANG[1], Jia-shi YANG[†‡1,3]

[1]Piezoelectric Device Laboratory, School of Mechanical Engineering and Mechanics, Ningbo University, Ningbo 315211, China

[2]School of Mechanical and Electrical Engineering, Ningbo Dahongying University, Ningbo 315175, China

[3]Department of Mechanical and Materials Engineering, The University of Nebraska-Lincoln, Lincoln, NE 68588-0526, USA

[†]E-mail: dujianke@nbu.edu.cn; jyang1@unl.edu

Received July 27, 2017; Revision accepted Jan. 25, 2018; Crosschecked Sept. 12, 2018

Abstract: We propose a new structure of ZnO or AlN thin film bulk acoustic wave filters using a ring-dot driving electrode operating with thickness-extensional modes. A theoretical analysis is performed to show the operating frequencies and modes of the proposed filter. The scalar differential equation by Tiersten and Stevens (1983) is used. An analytical solution is obtained. Numerical calculations based on the solution show that the vibration tends to be trapped in the electroded central and annular areas and decays away from the electrode edges. It is also shown that by properly designing the electrode dimensions and mass density, the nodal line of one of the two operating modes can be adjusted to lie in the gap between the ring and the dot driving electrodes which is ideal for a filter.

Key words: Piezoelectric; Thin film; Vibration; Resonator; Filter

https://doi.org/10.1631/jzus.A1700396   **CLC number:** TB51

1 Introduction

Acoustic wave resonators and filters made from piezoelectric crystals are key components in a lot of electronic equipment (Bottom, 1982; Salt, 1987). Electrical circuits such as oscillators with acoustic wave components are widely used as frequency standards and operators for time keeping and signal generation as well as processing. Conventional piezoelectric resonators and filters are made from crystals like quartz and lithium niobate, etc. They may operate with bulk (Bottom, 1982; Salt, 1987) or surface acoustic waves (Campbell, 1998; Hashimoto, 2000). During the last couple of decades, researchers

succeeded in depositing a very thin piezoelectric film of AlN or ZnO on a silicon layer to form thin film bulk acoustic wave resonators (FBARs) operating in the GHz frequency range (Lakin, 1999; Iriarte et al., 2002; Martin et al., 2006). FBARs have several advantages over conventional crystal resonators in filter applications (Lakin et al., 1995; Satoh et al., 2005). They have also been used to make acoustic wave sensors for mass and fluid sensing (Link et al., 2006; Fu et al., 2010; Zhang and Bao, 2014). Structurally, FBARs are multilayered plates with metal electrodes, a piezoelectric film, and an elastic substrate layer. The films can be lifted or solidly mounted on a substrate (Pang et al., 2005; Link et al., 2006). The c-axis of the material may be along the thickness or in-plane direction of the film, inclined in any direction, or zigzag in a multilayered film (Du et al., 2009; Qin et al., 2010; Zhang et al., 2010; Zhang and Kosinski, 2012; Zhang and Bao, 2014). FBAR materials and devices are of current and growing research interest experimentally, numerically, and theoretically (Jung et al., 2003; Gong et al., 2007; Buccela et al., 2008;

Campanella et al., 2009; de Santis et al., 2009; Katus and Reindl, 2010; Meltaus et al., 2012; Pan et al., 2012; Thakar et al., 2012; Wang et al., 2015).

Square (or rectangular) dielectric and piezoelectric layers as well as square electrodes have been routinely used for FBARs. It is known that electrode corners can cause electric field concentration (Yang et al., 2007) which is associated with degrading effects or even failure of the materials involved. In this paper, fundamentally different from the existing FBAR filters with rectangular electrodes (Tiersten and Stevens, 1983; Zhao et al., 2016a), we propose a new structure for an FBAR filter with circular geometry. It has a ring-dot driving electrode configuration. The proposed filter has a few advantages over filters with rectangular electrodes. The circular driving electrode does not have corners and the associated electric field concentration. A circular dot or ring electrode is also perfectly compatible with the in-plane material isotropy of AlN and ZnO. In addition, there is experimental suggestion that a circular thin film resonator has a higher quality factor (Kumar et al., 2016). We perform a theoretical analysis to obtain the basic vibration characteristics of the proposed filter.

2 Governing equations

Because of the material anisotropy of piezoelectric crystals and their electromechanical coupling, theoretical analyses of piezoelectric devices using the 3D theory of linear piezoelectricity present considerable mathematical challenges. Useful solutions can only be obtained in rare and special cases. To obtain theoretical results needed for the understanding and design of piezoelectric devices, various approximate techniques are necessary. For the most common FBARs with the c-axis of the material along the plate thickness, a single scalar differential equation was derived by Tiersten and Stevens (1983) for the operating mode, i.e. the transversely varying thickness-extensional mode in the device. The scalar equation itself is very simple and accurate. However, its derivation was very involved and one needs to go through a significant amount of algebra to calculate the coefficients of the equation in order to use it. As a consequence the equation has only been used in a few

studies (Zhao et al., 2015, 2016a, 2016b; Liu et al., 2017) with great successes. Recently, a summary of the expressions used to calculate the coefficients of the scalar equation was given in the appendix of Zhao et al. (2015), which made the use of the equation more convenient. The scalar equation is slightly different depending on whether there is a top driving electrode or not. For time-harmonic free vibrations of an FBAR at a resonance with a circular frequency ω which is to be determined, all fields have the same time dependence with a common factor $\exp(i\omega t)$ which will be dropped below. When there is no driving electrode, the nth-order thickness-extensional displacement u_3^n is approximately represented by Tiersten and Stevens (1983):

$$u_3^n \cong f^n(x_1, x_2) g^n(x_3), \tag{1}$$

where x_1 and x_2 are the in-plane coordinates of the plate. x_3 is the thickness coordinate. $g^n(x_3)$ is the field variation along the plate thickness. The in-plane field variation is described by $f^n(x_1, x_2)$ which is governed by Eq. (6.2) of Tiersten and Stevens (1983):

$$M_n\left(\frac{\partial^2 f^n}{\partial x_1^2} + \frac{\partial^2 f^n}{\partial x_2^2}\right) - \overline{c}_{33}^f \hat{\eta}_{f^n}^2 f^n + \rho^f \omega^2 f^n = 0. \tag{2}$$

Similarly, when there is a driving electrode, from Eq. (6.1) of Tiersten and Stevens (1983), the in-plane variation of the nth thickness-extensional mode is governed by

$$M_n\left(\frac{\partial^2 f^n}{\partial x_1^2} + \frac{\partial^2 f^n}{\partial x_2^2}\right) - \overline{c}_{33}^f \overline{\eta}_{f^n}^2 f^n + \rho^f \omega^2 f^n = 0. \tag{3}$$

M_n, $\overline{c}_{33}^f$, $\hat{\eta}_{f^n}^2$, and $\overline{\eta}_{f^n}^2$ in Eqs. (2) and (3) are independent of the spatial coordinates and are calculated according to Tiersten and Stevens (1983). ρ^f is the mass density of the ZnO film.

Along a curve separating a 2D region with a driving electrode and a region without a driving electrode, f^n and its normal derivative perpendicular to the curve must be continuous (Tiersten and Stevens, 1983). Denoting

$$\nabla^2 = \frac{\partial^2}{\partial x_1^2} + \frac{\partial^2}{\partial x_2^2} = \frac{\partial^2}{\partial r^2} + \frac{1}{r}\frac{\partial}{\partial r} + \frac{1}{r^2}\frac{\partial^2}{\partial \theta^2},$$

$$\overline{\omega}_n^2 = \frac{\overline{c}_{33}^f \overline{\eta}_{f^n}^2}{\rho^f}, \quad \hat{\omega}_n^2 = \frac{\overline{c}_{33}^f \hat{\eta}_{f^n}^2}{\rho^f}, \tag{4}$$

we rewrite Eqs. (2) and (3) in the following more compact form:

$$M_n \nabla^2 f^n + \rho^f (\omega^2 - \hat{\omega}_n^2) f^n = 0, \tag{5}$$

$$M_n \nabla^2 f^n + \rho^f (\omega^2 - \overline{\omega}_n^2) f^n = 0. \tag{6}$$

For circular devices we use polar coordinates defined by $x_1 = r\cos\theta$ and $x_2 = r\sin\theta$. Let the θ dependence of the fields be $\cos(m\theta)$, where $m = 0, 1, 2, \cdots$. Because of the in-plane material isotropy of ZnO and AlN, there is no need to consider the case of $\sin(m\theta)$. Then, for the plate with a ring-dot driving electrode configuration in Fig. 1, Eqs. (5) and (6) reduce to

$$M_n\left(\frac{\partial^2 f^n}{\partial r^2} + \frac{1}{r}\frac{\partial f^n}{\partial r} - \frac{m^2}{r^2}f^n\right) + \rho^f(\omega^2 - \overline{\omega}_n^2)f^n = 0,$$
$$r < R_0,$$

$$M_n\left(\frac{\partial^2 f^n}{\partial r^2} + \frac{1}{r}\frac{\partial f^n}{\partial r} - \frac{m^2}{r^2}f^n\right) + \rho^f(\omega^2 - \hat{\omega}_n^2)f^n = 0,$$
$$R_0 < r < R_1, \tag{7}$$

$$M_n\left(\frac{\partial^2 f^n}{\partial r^2} + \frac{1}{r}\frac{\partial f^n}{\partial r} - \frac{m^2}{r^2}f^n\right) + \rho^f(\omega^2 - \overline{\omega}_n^2)f^n = 0,$$
$$R_1 < r < R_2,$$

$$M_n\left(\frac{\partial^2 f^n}{\partial r^2} + \frac{1}{r}\frac{\partial f^n}{\partial r} - \frac{m^2}{r^2}f^n\right) + \rho^f(\omega^2 - \hat{\omega}_n^2)f^n = 0,$$
$$R_2 < r < \infty,$$

for the central region with a dot electrode, the gap between the dot and the ring electrodes, the annular region with a ring electrode, and the unelectroded outer region, respectively. For the so-called trapped modes we are interested in, the vibration outside an electrode decays away from the electrode edge, in particular when r approaches infinity. The boundary and continuity conditions are

$$f^n \text{ is finite}, \ r = 0, \tag{8a}$$

$$f^n(R_0^-) = f^n(R_0^+), \quad \left.\frac{\mathrm{d}f^n}{\mathrm{d}r}\right|_{R_0^-} = \left.\frac{\mathrm{d}f^n}{\mathrm{d}r}\right|_{R_0^+}, \tag{8b}$$

$$f^n(R_1^-) = f^n(R_1^+), \quad \left.\frac{\mathrm{d}f^n}{\mathrm{d}r}\right|_{R_1^-} = \left.\frac{\mathrm{d}f^n}{\mathrm{d}r}\right|_{R_1^+}, \tag{8c}$$

$$f^n(R_2^-) = f^n(R_2^+), \quad \left.\frac{\mathrm{d}f^n}{\mathrm{d}r}\right|_{R_2^-} = \left.\frac{\mathrm{d}f^n}{\mathrm{d}r}\right|_{R_2^+}, \tag{8d}$$

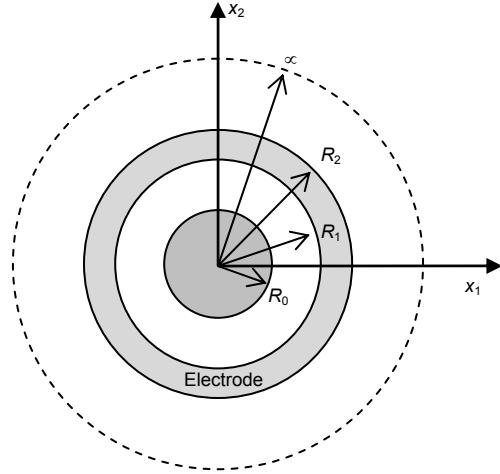$$f^n \to 0, \quad r \to \infty. \tag{8e}$$

Fig. 1 An FBAR filter with ring-dot driving electrodes

3 Analytical solution

We denote

$$\hat{\alpha}^2 = \frac{\rho^f(\hat{\omega}_n^2 - \omega^2)}{M_n} > 0, \quad \overline{\alpha}^2 = \frac{\rho^f(\omega^2 - \overline{\omega}_n^2)}{M_n} > 0. \tag{9}$$

Eq. (9) defines a frequency interval for the trapped modes of interest. Under the following separate transformations of the radial coordinate for the electroded and unelectroded regions:

$$\begin{aligned} \xi &= \overline{\alpha}r, & r < R_0, \\ \eta &= \hat{\alpha}r, & R_0 < r < R_1, \\ \xi &= \overline{\alpha}r, & R_1 < r < R_2, \\ \eta &= \hat{\alpha}r, & R_2 < r < \infty. \end{aligned} \tag{10}$$

Eq. (7) becomes

$$\frac{\partial^2 f^n}{\partial \xi^2} + \frac{1}{\xi}\frac{\partial f^n}{\partial \xi} + \left(1 - \frac{m^2}{\xi^2}\right)f^n = 0, \quad r < R_0, \tag{11a}$$

$$\frac{\partial^2 f^n}{\partial \eta^2} + \frac{1}{\eta}\frac{\partial f^n}{\partial \eta} - \left(1 + \frac{m^2}{\eta^2}\right)f^n = 0, \quad R_0 < r < R_1, \quad (11b)$$

$$\frac{\partial^2 f^n}{\partial \xi^2} + \frac{1}{\xi}\frac{\partial f^n}{\partial \xi} + \left(1 - \frac{m^2}{\xi^2}\right)f^n = 0, \quad R_1 < r < R_2, \quad (11c)$$

$$\frac{\partial^2 f^n}{\partial \eta^2} + \frac{1}{\eta}\frac{\partial f^n}{\partial \eta} - \left(1 + \frac{m^2}{\eta^2}\right)f^n = 0, \quad R_2 < r < \infty. \quad (11d)$$

Eqs. (11a) and (11c) and Eqs. (11b) and (11d) are the Bessel equations and modified Bessel equations of order m. The general solution to Eq. (11) satisfying Eqs. (8a) and (8e) can be written as

$$f^n = \begin{cases} A_1 J_m(\bar{\alpha}r), & r < R_0, \\ A_2 I_m(\hat{\alpha}r) + A_3 K_m(\hat{\alpha}r), & R_0 < r < R_1, \\ A_4 J_m(\bar{\alpha}r) + A_5 Y_m(\bar{\alpha}r), & R_1 < r < R_2, \\ A_6 K_m(\hat{\alpha}r), & R_2 < r < \infty, \end{cases} \quad (12)$$

where A_1–A_6 are undetermined constants. J_m and Y_m are the mth-order Bessel functions of the first kind and second kind, respectively. I_m and K_m are the mth-order modified Bessel functions of the first kind and second kind, respectively. The substitution of Eq. (12) into Eqs. (8b)–(8d) yields six linear homogeneous equations for A_1–A_6. For nontrivial solutions the determinant of the coefficient matrix of the equations has to vanish, which gives the frequency equation. The corresponding nontrivial solutions of A_1–A_6 determine the corresponding modes.

4 Numerical results and discussion

As a numerical example, consider a thin ZnO film filter operating with the fundamental thickness-extensional mode with $n=1$ and $m=0$ which are fixed throughout the rest of the paper. The thickness of the ZnO film is $h^f=5$ μm. The thickness of the silicon substrate is $h^s=5$ μm. The thickness of the Au driving electrode is $h'=0.044$ μm and that of the ground electrode is $h''=0.2$ μm. The corresponding mass ratios (Tiersten and Stevens, 1983) are $R'=0.03$ and $R''=0.1359$. The radii of the electrodes are that $R_0=150$ μm, $R_1=160$ μm, and $R_2=320$ μm. In this case, three roots are found in the frequency interval $(\bar{\omega}_1, \hat{\omega}_1)$ determined by Eq. (9). In terms of the frequency $f=\omega/(2\pi)$, they are: $f_1=365.5336$ MHz, $f_2=367.4778$ MHz, and $f_3=372.2517$ MHz, very close to each other because they are mainly determined by $n=1$ with a weak dependence on the in-plane mode variation. The three corresponding modes are shown in Figs. 2a–2c, respectively, in the order of increasing frequency. For better visualization, both a 3D plot and its cross-section along $x_3=0$ are shown for each mode. When the displacement of a mode vanishes at a line (point), the line (point) is called a nodal line (point). The three modes in Fig. 2 have zero, one, and two nodal lines, respectively. The thickness-extensional displacement with $n=1$ is essentially the thickness-extensional strain. If a nodal line is present in an electroded region, the strain changes its sign across the nodal line and so does the charge on the electrode produced by the strain through piezoelectric coupling. This causes charge cancellation on the electrode which reduces the capacitance and is usually undesirable for device applications. For the mode in Fig. 2b, the only nodal line is in the gap between the ring and dot electrodes, which is fine and desirable. However, for the mode in Fig. 2c, one of the two nodal line is within the dot electrode while the other is in the ring electrode. Therefore, the mode in Fig. 2c is not useful for the filter. When the plate is used as a filter, one of the ring-dot electrodes is with an input voltage for driving, and the other produces an output voltage. The filter can operate with the first mode in which the vibration of the entire plate is in phase. The second mode can also be used in which the regions with the dot and ring electrodes vibrate out of phase. When the frequencies of the two modes are close enough and their resonance peaks overlap to some degree, the two modes can be used together as a filter with essentially twice the bandwidth.

For filter design, the distance between the ring and the dot electrodes is crucial. If the distance is too large, the mechanical interaction between the vibrations under the two electrodes becomes less because of the decay of the vibration from electrode edges. In that case there is little output from the filter. In addition, it is desirable that the nodal line of the mode in Fig. 2b lies in the gap between the two electrodes. In Figs. 3 and 4 (p.791), the radius of the dot electrode, R_0, and the inner radius of the ring electrodes, R_1, are varied separately and thus changing the distance between the two electrodes. It can be seen that the modes are very sensitive to R_0 and R_1. Ideally we want

strong vibrations under both electrodes and there is a strong interaction between them. It can be seen that the vibration in the central region under the dot electrode is usually stronger than that in the annular region under the ring electrode. This in fact may be a good thing for the present circular filter because the ring electrode can be designed with a larger area than the dot electrode so that the charge on the ring electrode is comparable to that on the dot electrode although the vibration under the ring electrode is weaker.

Fig. 5 shows the effect of the outer radius of the ring electrode, R_2, on the two operating modes of the filter. For all of the modes, the vibration dies out sufficiently far away outside the ring electrode. This
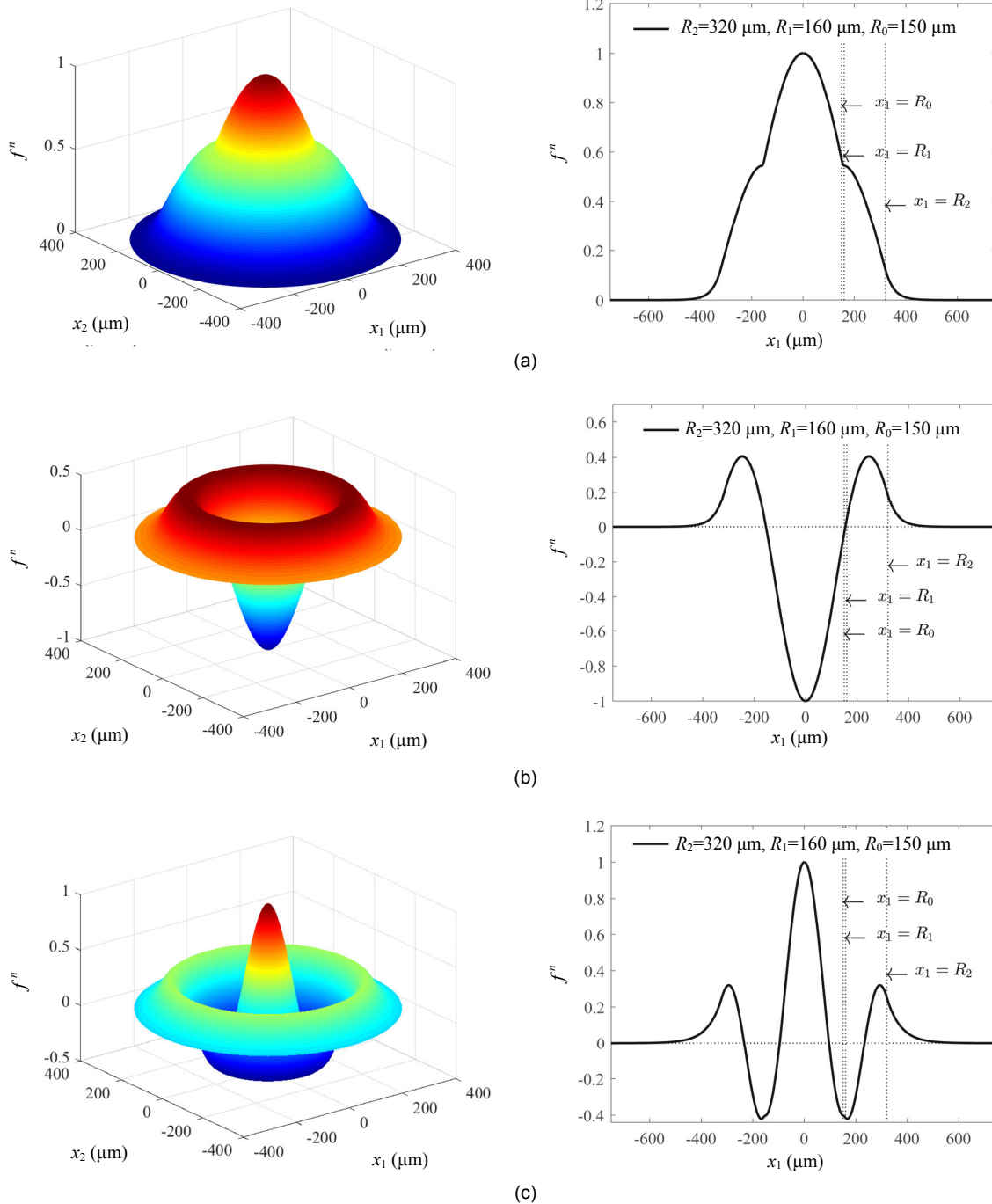

(a)

(b)

(c)

Fig. 2 Three trapped thickness-extensional modes. h^f=5 μm, h^s=5 μm, h'=0.044 μm, h''=0.2 μm, R'=0.03, R''=0.1359, R_0=150 μm, R_1=160 μm, R_2=320 μm. **(a)** f_1=365.5336 MHz; **(b)** f_2=367.4778 MHz; **(c)** f_3=372.2517 MHz

(a)   (b)
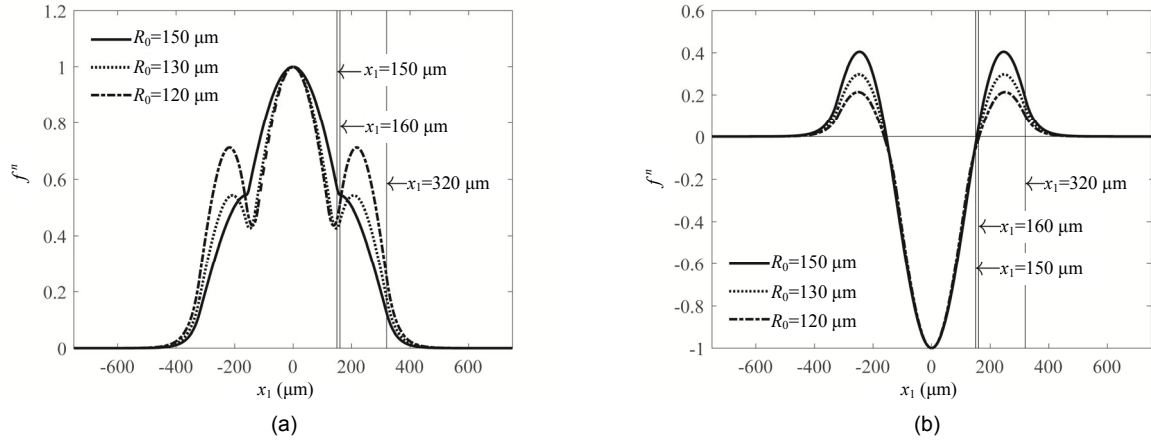
Fig. 3 Effects of the radius of the dot electrode, R_0, on the two operating modes. h^f=5 μm, h^s=5 μm, h'=0.044 μm, h''= 0.2 μm, R'=0.03, R''=0.1359, R_1=160 μm, R_2=320 μm. (a) R_0=150 μm, f_1=365.5336 MHz; R_0=130 μm, f_1=366.2273 MHz; R_0= 120 μm, f_1=366.4574 MHz; (b) R_0=150 μm, f_2=367.4778 MHz; R_0=130 μm, f_2=367.5586 MHz; R_0=120 μm, f_2=367.7180 MHz

(a)   (b)
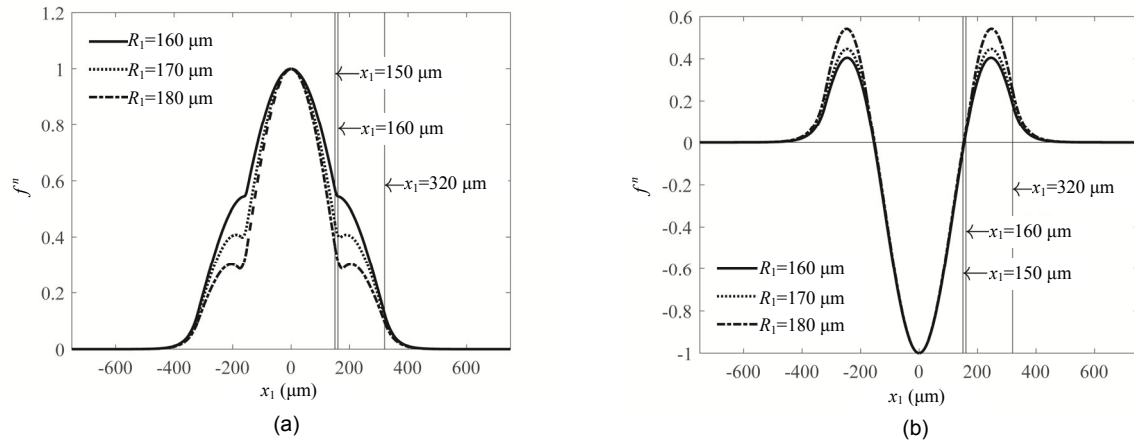
Fig. 4 Effects of the inner radius of the ring electrode, R_1, on the two operating modes. h^f=5 μm, h^s=5 μm, h'=0.044 μm, h'' =0.2 μm, R'=0.03, R''=0.1359, R_0=150 μm, R_2=320 μm. (a) R_1=160 μm, f_1=365.5336 MHz; R_1=170 μm, f_1=365.8962 MHz; R_1= 180 μm, f_1=366.1621 MHz; (b) R_1=160 μm, f_2=367.4778MHz; R_1=170 μm, f_2=367.4968 MHz; R_1=180 μm, f_2=367.5646 MHz

(a)   (b)
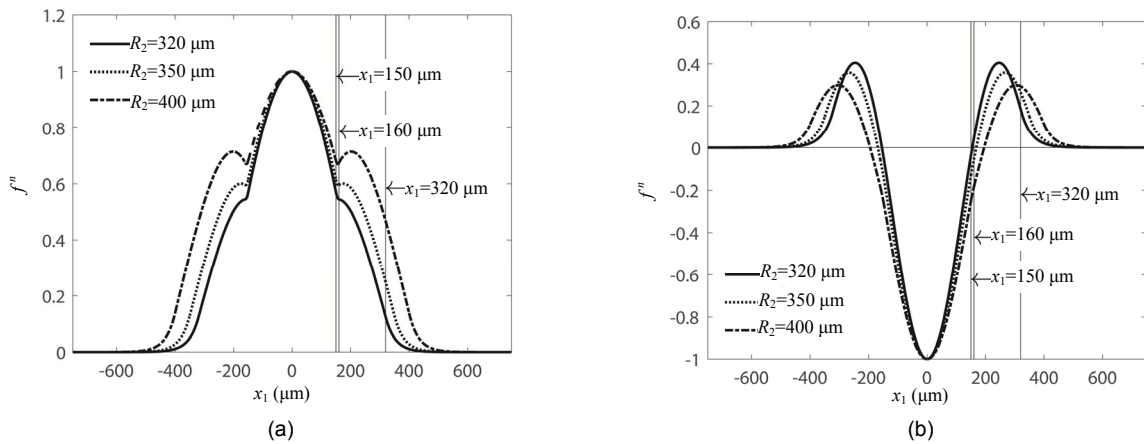
Fig. 5 Effects of the outer radius of the ring electrode, R_2, on the two operating modes. h^f=5 μm, h^s=5 μm, h'=0.044 μm, h'' =0.2 μm, R'=0.03, R''=0.1359, R_0=150 μm, R_1=160 μm. (a) R_2=320 μm, f_1=365.5336 MHz; R_2=350 μm, f_1=365.4076 MHz; R_2= 400 μm, f_1=365.2253 MHz; (b) R_2=320 μm, f_2=367.4778 MHz; R_2=350 μm, f_2=367.0491 MHz; R_2=400 μm, f_2=366.5753 MHz

is the so-called energy trapping of thickness-extensional modes. Energy trapping is crucial to device mounting which can be designed at the plate edges where there is little vibration so that mounting does affect device operation. R_2 is the main design parameter for energy trapping and it determines the size or boundary of a real and finite device. It can be seen that the modes are very sensitive to R_2.

In Fig. 6, all parameters are kept the same as those in Fig. 2 except that the driving electrode thickness is varied. Similarly, In Fig. 7, only the driving electrode material or effectively the driving electrode mass density is varied. According to Tiersten and Stevens (1983), the two effects in Figs. 6

and 7 affect the behavior of the filter in a combined manner through the mass ratio R' and cannot be separated within the approximate theoretical model of the scalar differential equations in Eqs. (2) and (3). It can be seen that the location of the nodal line and energy trapping of the thickness-extensional modes are both sensitive to the electrode thickness and density. Therefore, the electrode dimension and density are important design parameters.

In filter applications, instead of the frequencies of the two operating modes, i.e. f_1 and f_2, it is more convenient to use their average and difference. For convenience and comparison, we summarize the average frequency and the frequency difference of the
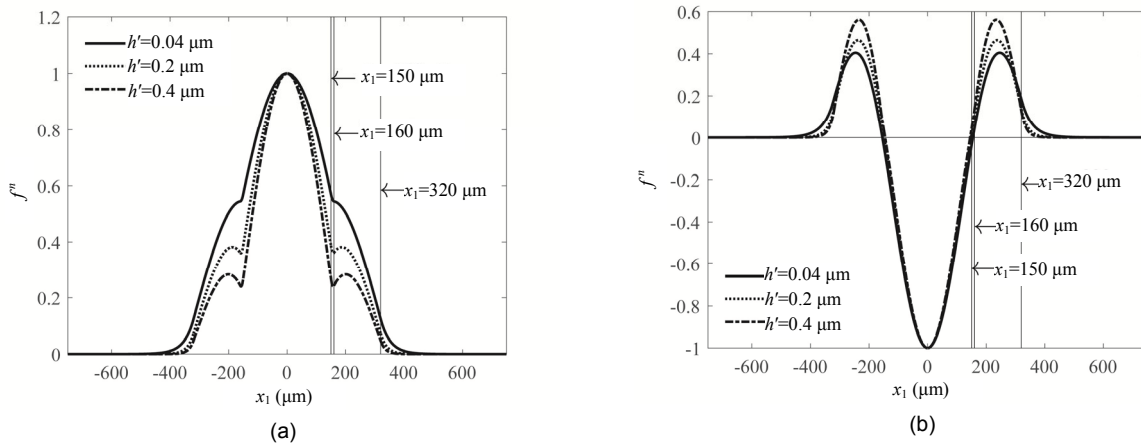

Fig. 6 Effects of the driving electrode thickness, h', on the two operating modes. h^f=5 μm, h^s=5 μm, h''=0.2 μm, R''=0.1359, R_0=150 μm, R_1=160 μm, R_2=320 μm. (a) h'=0.044 μm, f_1=365.5336 MHz; h'=0.2 μm, f_1=348.8182 MHz; h'=0.4 μm, f_1=327.1432 MHz; (b) h'=0.044 μm, f_2=367.4778 MHz; h'=0.2 μm, f_2=350.5370 MHz; h'=0.4 μm, f_2=328.6774 MHz
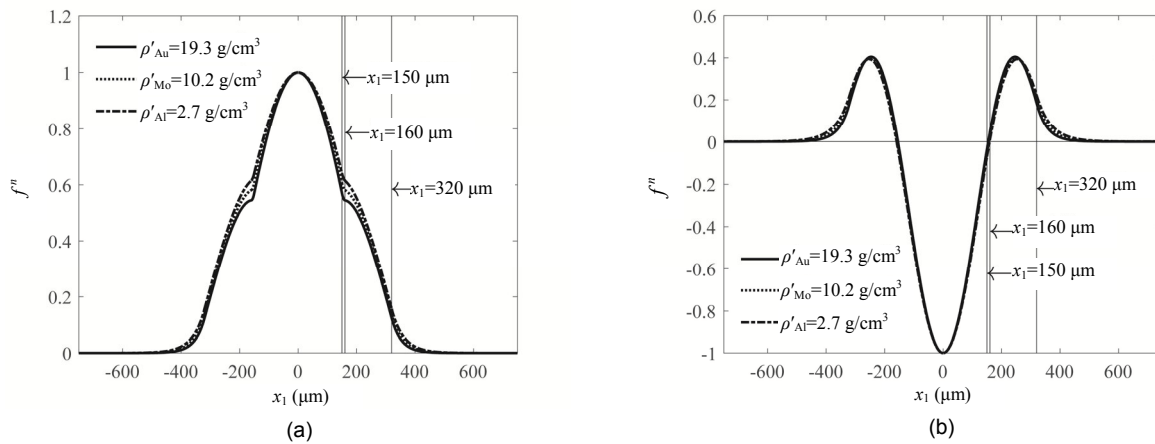
Fig. 7 Effects of the driving electrode mass density, ρ', on the two operating modes. h^f=5 μm, h^s=5 μm, h'=0.044 μm, h''=0.2 μm, R''=0.1359, R_0=150 μm, R_1=160 μm, R_2=320 μm. (a) ρ'=19.3 g/cm³, f_1=365.5336 MHz; ρ'=10.2 g/cm³, f_1=367.7326 MHz; ρ'=2.7 g/cm³, f_1=369.5376 MHz; (b) ρ'=19.3 g/cm³, f_2=367.4778 MHz; ρ'=10.2 g/cm³, f_2=369.6926 MHz; ρ'=2.7 g/cm³, f_2=371.4944 MHz

Table 1 Average frequency and frequency difference of the operating modes

R_0 (μm)	R_1 (μm)	R_2 (μm)	h' (μm)	ρ' (g/m³)	$(f_1+f_2)/2$ (MHz)	f_2-f_1 (kHz)
150	160	320	0.044	19.3	366.5057	1944.2528
130	160	320	0.044	19.3	366.8929	1331.3685
120	160	320	0.044	19.3	367.0877	1260.6349
150	170	320	0.044	19.3	366.6965	1600.5770
150	180	320	0.044	19.3	366.8634	1402.4924
150	160	350	0.044	19.3	366.2283	1641.4400
150	160	400	0.044	19.3	365.9003	1349.9358
150	160	320	0.200	19.3	349.6776	1718.8152
150	160	320	0.400	19.3	327.9103	1534.1840
150	160	320	0.044	10.2	368.7126	1959.9168
150	160	320	0.044	2.7	370.5160	1956.7986

modes in Figs. 2–7 in Table 1. The frequency difference is related to the width of the bandpass of the filter and needs to be designed according to the damping of the specific material used.

5 Conclusions

Within the narrow interval of $(\bar{\omega}_n, \hat{\omega}_n)$, there exist a few trapped modes with vibrations mainly under the dot-ring electrodes. With proper design, the nodal line of the second trapped mode lies in the gap between the ring and the dot electrodes. Then the first two trapped modes of the proposed structure can be used as the ideal operating modes for a filter. The location of the nodal line and the decay rate of the fields away from the electrode edges are sensitive to geometric and physical parameters. Therefore, these filters need to be designed accurately. The analysis in the present paper provides both basic understanding and design tools for these filters. Similar to the filter with interdigital electrodes in (Liu et al., 2017), circular FBARs with multiple ring electrodes can be used to make filters.

References

Bottom VE, 1982. Introduction to Quartz Crystal Unit Design. Van Nostrand Reinhold, New York, USA.

Buccela C, Santis VD, Feliziani M, et al., 2008. Finite element modelling of a thin-film bulk acoustic resonator (FBAR). *COMPEL-The International Journal for Computation and Mathematics in Electrical and Electronic Engineering*, 27(6):1296-1306.
https://doi.org/10.1108/03321640810905774

Campanella H, Martubcic E, Nouet P, et al., 2009. Analytical and finite-element modeling of localized-mass sensitivity of thin-film bulk acoustic-wave resonators (FBAR). *IEEE Sensors Journal*, 9(8):892-901.
https://doi.org/10.1109/jsen.2009.2024858

Campbell CK, 1998. Surface Acoustic Wave Devices for Mobile and Wireless Communications. Academic Press, Orlando, FL, USA.

de Santis V, Feliziani M, Buccella C, et al., 2009. Prototype design of a thin-film bulk acoustic-wave resonator by the finite element method. *IEEE Transactions on Magnetics*, 45(3):1116-1119.
https://doi.org/10.1109/tmag.2009.2012646

Du JK, Xian K, Wang J, et al., 2009. Thickness vibration of piezoelectric plates of 6 mm crystals with tilted six-fold axis and two-layered thick electrodes. *Ultrasonics*, 49(2):149-152.
https://doi.org/10.1016/j.ultras.2008.09.003

Fu YQ, Luo JK, Du XY, et al., 2010. Recent developments on ZnO films for acoustic wave based bio-sensing and microfluidic applications: a review. *Sensors and Actuators B: Chemical*, 143(2):606-619.
https://doi.org/10.1016/j.snb.2009.10.010

Gong X, Han M, Shang XL, et al., 2007. Two-dimensional analysis of spurious modes in aluminum nitride film resonators. *IEEE Transactions on Ultrasonics, Ferroelectrics, and Frequency Control*, 54(6):1171-1176.
https://doi.org/10.1109/tuffc.2007.370

Hashimoto KY, 2000. Surface Acoustic Wave Devices in Telecommunications. Springer, Berlin Heidelberg, Germany.
https://doi.org/10.1007/978-3-662-04223-6

Iriarte GF, Engelmark F, Katardjiev IV, 2002. Reactive sputter deposition of highly oriented AlN films at room temperature. *Journal of Materials Research*, 17(6):1469-1475.
https://doi.org/10.1557/jmr.2002.0218

Jung JH, Lee YH, Lee JH, et al., 2003. Vibration-mode

analysis of an RF film-bulk-acoustic-wave resonator by using the finite element method. *Journal of the Korean Physical Society*, 43(5):L648-L650.
https://doi.org/10.3938/jkps.43.648

Katus P, Reindl LM, 2010. Reduced order finite element models of bulk acoustic wave resonators. Proceedings of 2009 IEEE International Ultrasonics Symposium, p.2123-2128.
https://doi.org/10.1109/ultsym.2009.5441466

Kumar Y, Singh J, Kumari G, et al., 2016. Effect of shapes and electrode material on figure of merit (FOM) of BAW resonator. *AIP Conference Proceedings*, 1724:020045.
https://doi.org/10.1063/1.4945165

Lakin KM, 1999. Thin film resonators and filters. Proceedings of 1999 IEEE Ultrasonics Symposium, p.895-906.
https://doi.org/10.1109/ultsym.1999.849135

Lakin KM, Kline GR, McCarron KT, 1995. Development of miniature filters for wireless applications. *IEEE Transactions on Microwave Theory and Techniques*, 43(12):2933-2939.
https://doi.org/10.1109/22.475658

Link M, Schreiter M, Weber J, et al., 2006. Solidly mounted ZnO shear mode film bulk acoustic resonators for sensing applications in liquids. *IEEE Transactions on Ultrasonics, Ferroelectrics, and Frequency Control*, 53(2):492-496.
https://doi.org/10.1109/tuffc.2006.1593389

Liu J, Du JK, Wang J, et al., 2017. Long thickness-extensional waves in thin film bulk acoustic wave filters affected by interdigital electrodes. *Ultrasonics*, 75:226-232.
https://doi.org/10.1016/j.ultras.2016.12.004

Martin F, Jan ME, Rey-Mermet S, et al., 2006. Shear mode coupling and tilted grain growth of A1N thin films in BAW resonators. *IEEE Transactions on Ultrasonics, Ferroelectrics, and Frequency Control*, 53(7):1339-1343.
https://doi.org/10.1109/TUFFC.2006.1665082

Meltaus J, Pensala T, Kokkonen K, 2012. Parametric study of laterally acoustically coupled bulk acoustic wave filters. *IEEE Transactions on Ultrasonics, Ferroelectrics, and Frequency Control*, 59(12):2742-2751.
https://doi.org/10.1109/tuffc.2012.2515

Pan WL, Thakar VA, Rais-Zadeh M, et al., 2012. Acoustically coupled thickness-mode AIN-on-Si band-pass filters-part I: principle and devices. *IEEE Transactions on Ultrasonics, Ferroelectrics, and Frequency Control*, 59(10):2262-2269.
https://doi.org/10.1109/tuffc.2012.2451

Pang W, Zhang H, Kim ES, 2005. Micromachined acoustic wave resonator isolated from substrate. *IEEE Transactions on Ultrasonics, Ferroelectrics, and Frequency Control*, 52(8):1239-1246.
https://doi.org/10.1109/tuffc.2005.1509782

Qin LF, Chen QM, Cheng HB, et al., 2010. Analytical study of

dual-mode thin film bulk acoustic resonators (FBARs) based on ZnO and AlN films with tilted c-axis orientation. *IEEE Transactions on Ultrasonics, Ferroelectrics, and Frequency Control*, 57(8):1840-1853.
https://doi.org/10.1109/tuffc.2010.1623

Salt D, 1987. Hy-Q Handbook of Quartz Crystal Devices. Van Nostrand Reinhold, Wokingham, Berkshire, UK.

Satoh Y, Nishihara T, Yokoyama T, et al., 2005. Development of piezoelectric thin film resonator and its impact on future wireless communication systems. *Japanese Journal of Applied Physics*, 44(5A):2883-2894.
https://doi.org/10.1143/jjap.44.2883

Thakar VA, Pan WL, Ayazi F, et al., 2012. Acoustically coupled thickness-mode AIN-on-Si band-pass filters-part II: simulation and analysis. *IEEE Transactions on Ultrasonics, Ferroelectrics, and Frequency Control*, 59(10):2270-2277.
https://doi.org/10.1109/tuffc.2012.2452

Tiersten HF, Stevens DS, 1983. An analysis of thickness-extensional trapped energy resonant device structures with rectangular electrodes in the piezoelectric thin film on silicon configuration. *Journal of Applied Physics*, 54(10):5893-5910.
https://doi.org/10.1063/1.331763

Wang K, Koelle U, Larson JD, et al., 2015. FBAR laterally coupled resonator filter. Proceedings of 2015 IEEE International Ultrasonics Symposium, p.466-473.
https://doi.org/10.1109/ultsym.2015.0188

Yang JS, Xue H, Hu YT, 2007. Finite element analysis of stress field concentration near the edge of an electrode. *Ferroelectrics Letters Section*, 34(3-4):108-111.
https://doi.org/10.1080/07315170701500668

Zhang HF, Kosinski JA, 2012. Analysis of thickness vibrations of c-axis inclined zig-zag two-layered zinc oxide thin-film resonators. *IEEE Transactions on Ultrasonics, Ferroelectrics, and Frequency Control*, 59(12):2831-2836.
https://doi.org/10.1109/tuffc.2012.2526

Zhang HF, Bao YY, 2014. Sensitivity analysis of multi-layered C-axis inclined zigzag zinc oxide thin-film resonators as viscosity sensors. *IEEE Transactions on Ultrasonics, Ferroelectrics, and Frequency Control*, 61(3):525-534.
https://doi.org/10.1109/tuffc.2014.2936

Zhang HF, Turner JA, Kosinski JA, 2010. Analysis of thickness vibrations of c-axis inclined aluminum-nitrogen thin film resonators. *Integrated Ferroelectrics*, 113(1):95-108.
https://doi.org/10.1080/10584581003785476

Zhao ZN, Qian ZH, Wang B, et al., 2015. Energy trapping of thickness-extensional modes in thin film bulk acoustic wave resonators. *Journal of Mechanical Science and Technology*, 29(7):2767-2773.

https://doi.org/10.1007/s12206-015-0605-0

Zhao ZN, Qian ZH, Wang B, 2016a. Energy trapping of thickness-extensional modes in thin film bulk acoustic wave filters. *AIP Advances*, 6(1):015002.
https://doi.org/10.1063/1.4939695

Zhao ZN, Qian ZH, Wang B, 2016b. Vibration optimization of ZnO thin film bulk acoustic resonator with ring electrodes. *AIP Advances*, 6(4):045201.
https://doi.org/10.1063/1.4945732

中文概要

题　目： 具有环形-圆形电极的薄膜体声波滤波器

目　的： 研发一种新型氧化锌薄膜体声波滤波器，建模进行理论分析，并给出设计工具。

创新点： 提出一种氧化锌薄膜体声波滤波器的新结构。

方　法： 用 Tiersten-Stevens 方程进行理论分析与计算；方程及其求解和计算简单易行。

结　论： 具有环形-圆形电极的氧化锌薄膜可以作为体声波滤波器。圆形和环形电极具有简单和易加工等优点，并且工作模态的振动分布与材料的对称性高度一致，避免了矩形电极角点引起的电场集中等缺点。该滤波器的最优工作状态需要通过精密设计实现，本文提供了理论和计算设计工具。

关键词： 薄膜；声波；滤波器